

# Threshold and Hysteresis Effects in Wind Wave Growth and Decay. Part 1: Gravity-Capillary Waves

Mark A. Donelan<sup>1</sup>

Rosenstiel School of Marine and Atmospheric Sciences  
University of Miami  
Miami, FL 33149-1098 USA

William J. Plant

Applied Physics Laboratory, University of Washington  
Seattle, WA 98105-6698 USA

March 7, 2002

## Abstract

Measurements in a closed, recirculating wind wave tank using variable wind speeds have shown that wind waves in the gravity-capillary range exhibit threshold and hysteresis effects in their growth and decay. Surface wave height variance spectral densities in the wavenumber domain were measured for gravity-capillary waves using both radar backscatter and a wavelet transform technique applied to a laser probe. The measurements showed that when the wind speed was slowly ramped up and down, a threshold wind speed or friction velocity was required to produce waves. The threshold was different when the wind was increasing than when it was decreasing, leading to hysteresis in the observed spectral densities. Changing water temperature or current in the water caused a pronounced change in the wind speed threshold but not in the friction velocity threshold. Changes in fetch by as much as a factor of two had no discernible effect on the thresholds. By turning the wind on suddenly, holding it constant, then turning it off suddenly, initial growth rates of gravity capillary waves, their decay rates, and the time delay beyond the threshold wind speed when they began to grow could be determined. These studies showed that growth rates agreed well with previous results, that the waves decayed at two distinct rates, and that the time delay to growth was larger for smaller equilibrium wind speeds. These results indicate that wind input to gravity-capillary waves must exceed viscous damping before they can grow but that initial roughness is also necessary for growth. Thus growth is delayed beyond the minimum threshold wind speed while initial roughness develops, probably through the laminar-to-turbulent transition in the subsurface flow. Furthermore, the threshold for decay of gravity-capillary waves is reduced below the threshold for growth both because the delay awaiting roughness does not occur when waves are already present on the surface and because non-linear energy transfer supplies additional energy input. Finally, the results imply that wind speed, being a condition imposed on the air/water interface, causes wave growth while friction velocity, being a result of air/water interactions, is closely related to surface roughness and changes during wave growth.

---

<sup>1</sup>Also Scientist Emeritus, National Water Research Institute, Burlington, Ontario

# 1 Introduction

The initial growth of waves by the wind has been studied for many years, both theoretically (Jefferies, 1924, 1925; Miles, 1957, 1959a, 1959b, 1960, 1962; Valenzuela, 1976; Riley et al., 1982; Miles, 1993; Belcher and Hunt, 1993; Cohen and Belcher, 1999; Belcher, 1999) and experimentally (Shemdin and Hsu, 1967; Dobson, 1971; Elliot, 1972; Snyder, 1974; Larson and Wright, 1975; Wu et.al., 1979; Kawai, 1979, Snyder et.al., 1981; Plant, 1982; Kahma and Donelan, 1988). Recent work by Veron and Melville (2001) has shown that the initiation of wind waves is quickly followed by the development of Langmuir circulations. This work did not address the cause of the initial growth of the waves, however. In 1987, Donelan and Pierson suggested that short wind waves could not grow until the wind exceeded a threshold value at which the energy input from the wind could overcome dissipation due to viscosity (Donelan and Pierson, 1987). Thus, Donelan and Pierson predicted a very sharp rise from noise levels for short wave spectral densities at low winds. Because of the relationship between these spectral densities and radar cross sections of the ocean, they therefore predicted that these cross sections would also rise sharply from noise levels at low wind speeds. Initial attempts to detect this effect in wind wave tanks were not successful (Keller et al., 1995) but carefully controlled microwave measurements over the ocean have detected it (Plant et al., 1999a). In this paper we report the first observation of this threshold effect in a wind wave tank. Here we will limit ourselves to gravity-capillary waves with wavelengths of 1.51 cm (wavenumber = 415 rad/m) and 1.88 cm (wavenumber = 335 rad/m), Ku band microwave scatterers. These waves are never the dominant waves in our tank and we will show that their properties are independent of fetch. In a subsequent paper (Part 2), we will discuss the properties of longer waves nearer the dominant wavelength in the tank. We have observed the threshold effect in both microwave backscatter in the tank and in spectral densities obtained from a wavelet transform method applied to laser height/slope measurements made at a single point (Donelan et al., 1996). Furthermore, we show here that a similar threshold wind speed exists for the decay of wind waves with decreasing wind speed but that it is not always the same value as that for an increasing wind speed. That is, we report a hysteresis in the behavior of wave height variance spectral densities when the wind speed is cycled up and down in the tank. [Uz et al. (2002a) observed some hysteresis in laboratory wind waves forced by a sinusoidally modulated wind. There the hysteresis is ascribed to the finite response time of the waves as the wind rises and falls about some mean value well above the threshold]. In the experiment reported here the wind speed rises at a constant rate from zero through the threshold and then drops to zero at the same rate. We will show that this hysteresis results from a combination of a delay in decay, probably due to wave/wave interactions, and a delay in initial growth while surface roughness forms, probably as a result of the laminar to turbulent transition in the wind drift layer below the water surface.

Once this small, initial roughness is present on the water surface, past studies have shown that waves grow exponentially by amplification of the initial roughness. The two most commonly used forms for the exponential rate of growth of the waves are those given

by Plant (1982)<sup>2</sup>:

$$\beta = \frac{0.04u_*^2\omega}{c^2} \quad (1)$$

where  $u_*$  is friction velocity,  $c$  is the phase speed of the growing wave, and  $\omega$  is its angular frequency, and by Donelan and Pierson (1987):

$$\beta = K \left( \frac{\rho_a}{\rho_w} \right) \left[ \frac{U(\lambda/2)}{c} - 1 \right]^2 \omega \quad (2)$$

where  $K$  is an empirical constant which Donelan and Pierson determined from the data of Larson and Wright [1975] to be 0.194, and  $U(\lambda/2)$  is the wind speed at a height above mean water level of one half the wavelength of the growing wind wave. In Part 2, we will show that a better value for  $K$  is 0.17 and we will use this value in this paper.  $U(\lambda/2)$  is obtained from measurements of  $U$  and  $u_*$  at other heights  $z$  by

$$U(\lambda/2) = U(z) + \left( \frac{u_*}{\square} \right) \ln \left( \frac{\lambda}{2z} \right). \quad (3)$$

where  $\square$  is von Karman's constant, 0.4. Below we will show that by equating energy input by the wind to that lost to viscous dissipation, wave height variance spectral densities are obtained that are functions of the net growth rate, which is the sum of either of the above values of  $\beta$  and viscous dissipation,

$$\beta_d = -4\nu k^2 \quad (4)$$

where  $k$  is water wavenumber.

For wavelengths less than a few tens of centimeters, (1) and (2) yield growth rates so close together that it is difficult to distinguish between them by comparison with measured growth rates (Donelan and Pierson, 1987). Here, we attempt to discriminate between them by observing the behavior of the threshold wind speed and friction velocity for different water temperatures. We also examine the behavior of the threshold wind when current is present in the water.

## 2 Experimental Design

Figure 1 shows the experimental setup. The scanning laser slope gauge shown in the figure was not used in the measurements reported here. Some runs were made with the surface covered for a distance of 5 meters, shortening all indicated fetches by this amount. In all cases, care was taken that the airflow made a smooth transition to the water. The microwave

---

<sup>2</sup>Measurements in the same laboratory in 1993 using a scanning laser slope gauge (Uz et al., 2002b) are in close agreement with the empirical constant 0.04 in (1)

antennas were directed both upwind and downwind and were set at incidence angles of  $35^\circ$  and  $45^\circ$ . When the antennas looked upwind, the microwave footprint on the water was at a fetch of 5 or 10 m. Looking downwind, the fetches were 7.4 and 12.5 m. The inside roof and sides of the wind tunnel were lined with microwave absorbing material to a distance of 2.4 m upwind and 1.8 m downwind from the Teflon window. The width of the tank was 76 cm. The wind was varied in two modes, "ramped" and "sudden start and stop", which will be described below.

The point height/slope gauge shown in Figure 1 consisted of an Argon-Ion (488 nm – blue) laser transmitting 2 W of power whose beam was directed upward through the water surface. Fluorescein in the water caused the beam, which is blue in air, to fluoresce, producing a green beam (513 nm) in the water. A line-scan camera observing the surface spot from above through the side of the tank tracked the vertical movement of the surface spot. A green filter over the lens discriminated against the blue beam above the water surface. A Fresnel lens and 4-quadrant detector above the tank recorded the position of the laser beam after it was refracted by the water surface. The gauge detected all frequencies of motion of the surface up to a maximum determined by the spot size of the beam on the water surface and by the sampling frequency, which was 1000 Hz for the measurements reported here. However, signal-to-noise problems in fact limit the frequency response to a value somewhat lower than this. The spot size was about 1 mm, so wavenumbers up to about 3000 rad/m could be measured. The maximum slope that could be measured by the system was  $42^\circ$ . As outlined in more detail below, complete wave height variance spectra as a function of wavenumber and frequency,  $F(\vec{k}, \omega)$ , could be obtained from this gauge after processing.

The microwave system was identical to that described in detail by Plant et al. [1994] except that the frequency had been shifted up to Ku band; it is exactly the same system used by Plant et al. [1999b]. Briefly, the system was a coherent, dual-polarized, continuous wave system and data were collected on horizontal transmit/horizontal receive (HH) and vertical transmit/vertical receive (VV) polarizations simultaneously. Exact frequencies were 14.00 GHz for VV and 14.06 for HH. One-way half-power antenna beamwidths were  $6.6^\circ$  in the E plane and  $5.0^\circ$  in the H plane, and the beam viewed the water surface through a 6 mm thick Teflon window. The height of the antennas was maintained at 146 cm above mean water level for all incidence angles and look directions. Calibration procedures differed slightly from those described by Plant et al. [1994] owing to the laboratory setting. Water was drained from the tank, and a corner reflector was placed on absorbing material on the bottom of the tank at various positions in the beam. Return from the corner reflector was measured as a function of position in the beam and used to calculate calibration constants as described by Plant et al. [1994]. In addition, illuminated areas could be calculated since return power as a function of position was measured. We found these areas to be accurately given by

$$A = \pi a^2 / \cos \theta \quad (5)$$

where  $\theta$  is incidence angle and  $a$  is 13 cm for VV and 15 cm for HH polarization. Microwave return was collected at a sample rate of 257 Hz to fill an array 1024 samples long in 4 s

during the ramped runs. In the sudden start and stop runs, the sample rate was 1042 Hz for the same array size, yielding a measurement every 0.98 sec. This array was then Fourier transformed to produce Doppler spectra that were stored on optical disks. A reference signal from the microwave system and the mean value of the sum of the squares of the in phase and quadrature channels were stored for later use in computing normalized radar cross sections  $\sigma_o$ . Only these cross sections are of interest in this paper.

Winds in the tank were measured using a Pitot tube and hot X-film anemometers, from which friction velocities could be calculated. The height of the Pitot tube varied from 3 to 8.1 cm above the water surface during the experiments, and the hot film was 3.2 cm directly above the Pitot tube. The Pitot tube was used to calibrate the X-film anemometers several times per day by ramping the wind speed up and down. The X-film anemometers were then used to determine the horizontal mean wind speed and fluctuations of both horizontal and vertical components of the wind. From these the friction velocity at the height (usually 3 cm) of the X-film anemometers  $u_*(z)$  was calculated. Wind speeds shown in figures in this paper have been adjusted to be those at a 3 cm height, except in the time plots where measured wind speeds are shown. Friction velocities quoted here have been corrected to be those at the surface. The experimentally determined correction was

$$u_*^2(0) = \left[ \frac{25}{25 - z} \right]^2 u_*^2(z) \quad (6)$$

where  $z$  is the height of the measurement in cm (Uz et al., 2002a). Note that the change of  $u_*$  is small in the region below 3 cm, so that a constant flux approximation is appropriate in deducing the velocity profile at lower heights. Air and water temperatures were recorded during each run, and the water surface was skimmed free of surfactants each morning before the runs began. The wind measurements were recorded on a different computer from the radar measurements. However a synchronizing signal, a 30 second saw tooth, was recorded on both computers as was the signal from the Pitot tube. The Pitot tube signals recorded on the two computers were plotted together to verify synchronization. As noted above, winds were varied in two ways. In the mode we will call "ramped", the wind speed was increased linearly to a maximum value then linearly decreased at the same rate. We will specify these wind ramps in terms of the maximum value of wind speed and either the constant magnitude of the acceleration of the wind or the time length of the run. The second mode we will call the "sudden start and stop" mode. Here the fan was turned on suddenly and held at a constant speed until it was suddenly turned off. The wind speed had a rise and decay time that will be shown in the figures but was generally near equilibrium by the time waves began to grow and decayed rapidly relative to the time over which the waves decayed.

### 3 Wavenumber Spectra

Along with wind speed and friction velocity, the wave height variance spectrum as a function of wavenumber,  $F(k_x, k_y)$ , where  $k_x$  is the along-tank wavenumber and  $k_y$  is the cross-tank wavenumber, was central to this study. We measured  $F(k_x, k_y)$  using both radar backscatter

and a wavelet technique applied to the output of the laser gauge. We then compared these data to simple, first-order models of the behavior of  $F(k_x, k_y)$ .

### 3.1 Spectra from Radar Backscatter

At sufficiently low wind speeds, radar backscatter from rough water surfaces is Bragg scattering. Under these circumstances, the relationship between the radar cross section,  $\sigma_o$ , and  $F(k_x, k_y)$  is given by

$$F(2k_o \sin \theta_i, 0) = \frac{\sigma_o}{16\pi k_o^4 \cos^2 \theta_i |g_{qp}|^2} \quad (7)$$

where  $g_{pq}$  is a function of incidence angle and dielectric constant depending on polarization,  $(p, q)$ ,  $\theta_i$  is incidence angle, and  $k_o$  is the wavenumber of the microwave radiation. Expressions for  $g_{pq}$  are given by Plant [1990].

This expression does not work well at higher wind speeds where the more complex composite surface scattering theory must be used. Our concern in this paper, however, is primarily with the growth and decay of wind waves near the threshold wind speed, which is low. Thus we always relate spectral density  $F$  to cross section  $\sigma_o$  by (7) in this paper.

### 3.2 Spectra From Laser Height and Slope Measurements

Radar backscatter yields  $F(k_x, k_y)$  only for a very small range of wavenumbers around  $(2k_o \sin \theta_i, 0)$ , the Bragg wavenumber. By contrast, a wavelet technique developed by Donelan et al., [1996] yields  $F$  for all values of  $(k_x, k_y)$ . In these experiments, this technique was applied to height/slope measurements made by the laser at a single point by expanding the surface displacement in a Taylor series about the point of measurement. Given the slopes in the along and cross tank directions, the first two terms in the series may be evaluated, effectively yielding wave amplitude measurements at four points, two in each the along and cross tank directions. To ensure that the effect of curvature and higher order terms is relatively small, the separation,  $\delta$ , of these virtual probes from the location of the height measurement needs to be small: setting  $\delta < 0.1/k_{max}$ , where  $k_{max}$  is the highest wavenumber to be investigated, reduces the curvature contribution to less than 5 per cent of the slope contribution to elevation at the virtual probes. We set  $k_{max}$  to 600 rad/m and  $\delta$  to 0.01 mm. Comparisons with duplicate runs using  $\delta$  of 0.05mm showed no perceptible difference. Applying wavelet techniques to the outputs of these four virtual probes then yields time series of wave heights in various, non-overlapping frequency bands. Phase differences,  $\Delta\phi_i$  and separations  $\vec{r}_i = (r_i, \alpha_i)$  between pairs of probes at  $90^\circ$  to each other then yield the instantaneous wavenumber and direction,  $\phi$ , associated with each frequency according to the following equations:

$$k = \frac{r_2 \Delta\phi_1 \sin \alpha_2 - r_1 \Delta\phi_2 \sin \alpha_1}{r_1 r_2 [\sin(\alpha_2 - \alpha_1) \cos \phi]} \quad (8)$$

$$\phi = \tan^{-1} \left[ \frac{r_2 \Delta \phi_1 \cos \alpha_2 - r_1 \Delta \phi_2 \cos \alpha_1}{r_1 \Delta \phi_2 \sin \alpha_1 - r_2 \Delta \phi_1 \sin \alpha_2} \right] \quad (9)$$

Taking the squared magnitude of the wave amplitude in each frequency band and averaging many such individual measurements yields the wave height variance spectrum as a function of wavenumber for each frequency band. That is, it yields the complete variance spectrum of the wave height as a function of  $(k_x, k_y, \omega)$  where  $\omega$  is angular frequency. Integration over  $\omega$  then yields  $F(k_x, k_y)$ .

### 3.3 Spectra During Growth, Decay, and Equilibrium

The initial growth of wind waves has been shown to be exponential over a wide range of conditions so we use the following form to fit the initial growth:

$$F(k_x, k_y) = F_o e^{(\beta + \beta_d)t} \quad (10)$$

where  $F_o$  is the initial roughness and  $t$  is time. Note that nearly all theories of wave growth require that an initial roughness be present in order for wind waves to grow on water surfaces. In other words, the growth process is really an amplification process. Note also that when the wind is reduced to zero, spectral densities decay exponentially to zero at the viscous dissipation rate in the absence of other energy transfers.

A first-order form for  $F(k_x, k_y)$  when the waves are in equilibrium was developed by Plant [1986] by equating energy input from the wind to that dissipated by viscosity; a similar technique was used by Donelan and Pierson [1987]. Plant's result may be derived simply as follows. On dimensional grounds, we may write the following relation between wind input and dissipation:

$$(\beta + \beta_d)(k^4 F) = \omega f(k^4 F) \quad (11)$$

where  $f(k^4 F)$  is an unknown function describing total dissipation. Since  $k^4 F$  is small, we expand about an even smaller noise level to second order to get

$$(\beta + \beta_d)(k^4 F) = \omega [a_o + a_1(k^4 F) + a_2(k^4 F)^2] \quad (12)$$

Since the equation must be satisfied when  $F = 0$ ,  $a_o = 0$ . The term involving  $a_1$  is an eddy viscosity term which may be included in  $\beta_d$  if it is significant. Ignoring this term yields,

$$F(k_x, k_y) = \frac{(\beta + \beta_d)}{a_2 \omega k^4}. \quad (13)$$

Past work has indicated that  $a_2 = 20$  is a good approximation to the coefficient of the second order dissipation term.

Of course, one expects the order of dissipation to be about the same as the order of the non-linear interaction (Phillips, 1985) so this simple model must be extended to higher

orders for waves well into the gravity wave range. We apply it below to radar backscatter from surface waves 1.51 and 1.88 cm in length.

Donelan and Pierson [1987] applied similar energy balance considerations to deduce  $F(k_x, k_y)$ . They let  $f(k^4 F) = (k^4 F)^{n+1}$  and obtained:

$$F(k_x, k_y) = k^{-4} \left[ \frac{(\beta + \beta_d)}{\alpha \omega} \right]^{\frac{1}{n}}. \quad (14)$$

They obtained the parameters  $\alpha$  and  $n$  from a combination of wave group considerations and data fitting. They assumed that these parameters vary with position in the capillary gravity range and have the same fixed values for both pure gravity and pure capillary waves. They found that

$$\ln \alpha = 17.4 \left| 2 - \frac{g + 3\gamma k^2}{g + \gamma k^2} \right|^3 + 4.6; \quad n = 3.85 \left| 2 - \frac{g + 3\gamma k^2}{g + \gamma k^2} \right|^3 + 1.15 \quad (15)$$

where  $g$  is the acceleration due to gravity and  $\gamma$  the surface tension.

Below, we will compare our measured  $F(k_x, k_y)$  values both with Donelan and Pierson's predictions by combining 2 and 14 and with Plant's predictions by combining 1 and 13.

## 4 Ramped Winds

The range of threshold wind speeds for the wavenumbers accessible to our methods is not large and an experiment in which the wind speed is altered in steps may well miss the interesting transitions that occur at the threshold. Consequently, we elected to conduct a series of experiments in which the wind speed was varied by computer control: increasing from zero to some preset maximum value at a fixed rate and then decreasing to zero again at the same rate. In this way the threshold effects could be observed with great precision. Several variations of measurement were possible while ramping the wind speed up and down. We varied the rate of change of the wind, the temperature of the water, and the current in the water. Our standard slow ramp increased the wind speed at a rate of about 0.3 cm/s/s while three faster ramps increased it at about 0.8, 2.7, and 3.7 cm/s/s. We varied the water temperature from about 20°C to 30°C. Pumped currents in the direction of the wind ranged from 0 to about 30 cm/s.

### 4.1 Slowly Ramped Winds

Figure 2a shows a time series of wind speed and friction velocity obtained with a slowly ramped wind speed whose rate of change was 0.34 cm/s/s. Air and water temperatures were 21.9°C and 21.2°C, respectively, during this run and no current was used. Figure 2b shows the corresponding time series of spectral densities obtained from the radar (lines) and laser (symbols) at an along-tank wavenumber of 335 rad/m. The radar data were taken at a 35°



incidence angle looking upwind so the fetch was 10 m; laser data were at 14.3 m fetch. The striking feature of these spectral densities is that they rise and fall only when some threshold wind speed or friction velocity is reached. The agreement between the two measurements for wind speeds near and just above the threshold gives confidence that both instruments are indeed measuring short wave spectral densities. The figure shows that spectral densities from the radar are significantly above those from the laser at high wind speeds. This is because the radar backscatter is no longer the simple Bragg scattering described above at these wind speeds. Rather it must be described by composite surface theory where the scattering is modified by tilting and modulation of free and bound short waves by longer ones (Plant et.al., 1999b). Note that spectra derived from the vertical transmit/vertical receive (VV) radar mode are nearly identical to those from the horizontal transmit/ horizontal receive (HH) mode near the threshold. Thus in most of the following figures, we will show only the VV mode.

Figure 3 shows measured radar cross sections for VV polarization and waveheight spectral densities from the laser for the run shown in Figure 2 plotted versus wind speed and friction velocity. The threshold near a wind speed (at 3 cm height) of 1.8 m/s or a friction velocity of 0.08 m/s is clearly shown in the figure for both rising and falling winds. The solid lines are cross sections and spectral densities according to (13) for  $\beta$  given by (1) using measured friction velocities; the dashed lines are the same but using (14) and  $\beta$  from (2). Cross sections and spectral densities are related via (7). Clearly, the threshold occurs very near the wind speed at which wind input overcomes viscosity. However, thresholds predicted by the Plant growth rate are always too high; we will return to this point later. Also note that the Plant formulation of  $F(k_x, k_y)$ , (13), is closer to the measured values at the higher wind speeds than is that of Donelan and Pierson, (14).

## 4.2 Changes of Fetch and Ramp Rate

So far we have concentrated on our slowest ramp rates and have seen only small indications of hysteresis in the plots of spectral density versus wind. We view this again in Figures 4 and 5 but at a wavenumber of 415 rad/m and a variety of fetches. This variety is possible because we have combined upwind and downwind radar looks, with and without the water surface mask, with the laser data. Figure 4 shows increasing wind speeds while Figure 5 shows decreasing ones; the ramp rate in these figures is 0.3 cm/s/s. Figures 6 and 7 show similar results for a faster ramp rate of 2.7 cm/s/s. All of these figures clearly show that neither the threshold wind speed nor the spectral densities at higher wind speeds of waves with wavenumber 415 rad/m depends on fetch. If propagation of waves down the tank were a factor determining the wind speed threshold in Figure 6, then the data at 14.3 m fetch would have a threshold that was 0.4 m/s higher than that of the data at 10 m fetch, assuming a propagation speed for the waves of 0.3 m/s. Since this is obviously not the case, the possibility of advective effects playing a role in determining the thresholds is ruled out. Note, however, that the threshold, say at  $\sigma_o = -50$  dB for increasing wind speed at this faster ramp rate (Figure 6) is higher than that for the slower ramp rate (Figure 4). Similarly

the threshold for decreasing wind speed at the faster ramp rate (Figure 7) is much lower than that for the slower ramp rate (Figure 5).

This hysteresis effect was observed in all of our data for ramp rates above 0.5 cm/s/s. Since fetch does not play a role in the hysteresis, we suggest that two effects may be responsible for it. First, the waves cannot grow initially even when wind input can overcome viscosity until some initial roughness is present on the surface at that wavenumber. In Section 6 we will demonstrate that a possible source of this initial roughness is the laminar-to-turbulent transition of the subsurface flow (Caulliez et al., 1998). Thus we postulate that the threshold wind speed may increase for rapidly increasing winds due to the delay caused by the finite time necessary for this transition to occur. For rapidly decreasing winds, this increase in threshold would not occur because roughness is already present. In any case, this effect could not explain the delay, or shift to lower wind speeds, of the threshold for decreasing winds as the ramp rate increases. Rather, we suggest that a second effect is involved in the observed hysteresis. For decreasing wind speeds, energy transfer from longer waves to the gravity-capillary waves must augment wind input to maintain these waves against viscosity. In Section 5 we will provide additional evidence for this proposition.

### 4.3 Changes of Water Temperature

We made runs at water temperatures near 20°C and 30°C. Plots of radar cross section versus friction velocity and wind speed at the two temperatures are shown in Figure 8 for a slowly decreasing wind. As the water temperature increases, the viscosity of water decreases, and the expected threshold should shift to lower values. Figure 8 shows that this occurs when cross section is plotted against wind speed but not when it is plotted against friction velocity. This result suggests that the wind speed near the surface, not the friction velocity, is the determining factor in wave growth. The growing waves change the friction velocity in such a way that its value at threshold remains constant. This is consistent with the observation, pointed out above, that the friction velocity threshold predicted using Plant's growth rate is higher than observed. Before the waves grow, the friction velocity is very near the smooth flow value of about  $U/25$  and is too small to cause (1) to yield growth rates larger than the viscous dissipation rate. Only when the waves have already grown is the friction velocity high enough that (1) yields values above the dissipation rate. In fact, in the small fetches of this laboratory experiment the short waves, to which the radar responds, are the roughness elements in light winds near the threshold. Consequently, once these waves start growing in a slowly increasing wind, they cause the air boundary layer flow to transition from smooth to rough and produce a sudden increase in the friction velocity. In examining the rapid the rapid changes in wave energy near the threshold wind speed the imposed wind speed is the cause and the rapid growth of the short waves, the effect. In turn the waves roughen the surface and cause an accelerated increase of the friction velocity.

Our measurements clearly imply that in this wave tank setting the radar cross section near the threshold friction velocity is directly related to the friction velocity. In an ocean setting, longer waves would usually be present to disrupt this relationship. In fact, Plant

et al. (1999a) showed that on the ocean the radar cross section does not follow the friction velocity at low winds as well as it does at high ones.

#### 4.4 Changes due to Currents

The changes in the threshold wind speed and friction velocity caused by changes in current are illustrated in Figure 9. Again the decreasing part of the wind speed ramp is used and the ramp rate was at its lowest value. Here we plot radar cross section at a  $45^\circ$  incidence angle (Bragg wavenumber = 415 rad/m) versus either wind speed or friction velocity for currents of 0, 12, and 27.6 cm/s in the same direction as the wind. Increasing the current clearly increases the threshold wind speed but changes the threshold friction velocity little. The increased wind speed threshold, however, is larger than the currents used: going from zero current to 12 cm/s increases the threshold by 41 cm/s while going from 0 to 27.6 cm/s increases it by 59 cm/s. If the current were laminar, one would expect that wave growth would occur whenever the wind relative to the moving water exceeded the constant threshold. Thus the threshold in the laboratory reference frame would increase by the amount of the current. But the current is obviously turbulent as evidenced by the increase in cross section below the threshold. The fact that the threshold increases more than expected when starting from zero current suggests that the eddy viscosity associated with this turbulence increases the dissipation of the waves. Thus a larger wind speed relative to the moving water surface is required to maintain waves than would be required in the absence of turbulence. This suggestion is supported by the fact that the change in threshold when going from a current of 12 cm/s to one of 27.6 cm/s is 18 cm/s, very nearly the current increment. This is what one would expect if the turbulence level were not very sensitive to the current level once it is nonzero. The slight decrease in spectral density above the threshold wind speed also supports the idea of turbulent damping. These results do not contradict the assertion that the aqueous shear flow must change from laminar to turbulent in order for waves to grow. Small amounts of turbulence are required to generate the initial roughness but increasing the level of turbulence increases the dissipation (See Veron and Melville, 2001), causing short waves to be damped. These measurements clearly show that a given level of radar cross section will be related to a different wind speed depending on the current in the water. The relationship between radar cross section and wind stress appears to be little affected by currents, however.

### 5 Winds Suddenly Started and Stopped

By suddenly starting and stopping the tank fan, we were able to observe the initial growth of gravity-capillary waves and their decay when the wind was suddenly reduced to zero. While neither the starting nor stopping of the wind was instantaneous, it was sufficiently sudden to insure that the waves usually grew in winds that were very near their equilibrium values.

## 5.1 Development of the Wind Stress

Figure 10 and 11 show time series of wind speed, friction velocity, and spectral densities from both the radar and laser as the wind was suddenly accelerated, held constant, then suddenly dropped to zero. The Bragg wavenumber is 335 rad/m. In Figure 10, the equilibrium wind speed is 5.5 m/s while in Figure 14, it is 2.7 m/s. Again, we have excellent agreement between spectral densities derived from radar and laser measurements while the waves are growing and decaying. Heavy dashed lines in the figures indicate the growth predicted using (10) and Donelan and Pierson's growth rate, (2), heavy solid lines are the same using Plant's growth rate, (1), and dash-dotted lines indicate viscous decay. Figure 10 shows that the wind is within 20% of its final value during the last two decades of the initial Bragg wave growth. The friction velocity does not reach its equilibrium value, however, for almost 30 seconds after the wind has reached its maximum value. In fact during the period of wave growth, the friction velocity is less than one-third of its maximum value. Thus when the wind starts suddenly, short wind waves may not grow in a friction velocity environment that is the same as that at equilibrium as most theories of wave growth assume. The numbers change for lower maximum wind speeds. In Figure 11, where the maximum wind speed is 2.7 m/s, the wind speed has reached its maximum value during the last two decades of wave growth; friction velocity continues to increase slowly until the waves saturate. These observations again indicate that the level of the friction velocity is established by the waves once they are present.

## 5.2 Parameters of Growth and Decay

Runs such as those shown in Figures 10 and 11 allowed us to investigate growth and decay rates of waves with wavenumbers 335 and 415 rad/m in some detail. Since the radar data in these figures were taken at a fetch of 10 m and the laser data were taken at 14.3 m, their agreement once again provides evidence of the local nature of the processes being observed. Of particular interest was the slow decay, at a rate below that of viscous decay, that is evident in both figures. We fit straight lines to the data during both the growth and decay phases and determined growth and decay rates from their slopes. The results are shown in Figure 12. Figures 12a and 12b show decay rates measured at our two wavenumbers along with the viscous decay rate as a solid line. Clearly the faster decay is due to viscosity. The slow decay, interestingly enough, appears to be at about a quarter of this rate. This is consistent with the viscous decay rate of a wave twice as long as the Bragg wave. This suggests that some of our observed gravity-capillary waves are bound to longer waves and decay with them, an example of a non-linear interaction. Measured growth rates are compared with those predicted by Donelan/Pierson and by Plant in Figures 12c and 12d. Both growth rate formulations are within a factor of two of the measured rates, offering no clear evidence as to which is preferable.

## 6 Prediction of the Laminar-to-Turbulent Transition of the Drift Current

One other feature of the growth of gravity-capillary waves is evident in Figures 10 and 11: at the different equilibrium wind speeds, the difference in the time delay between the wind reaching the threshold value and the appearance of the waves. This difference, we suggest, is due to the time required for the sub-surface layer to reach the laminar-to-turbulent transition. Caulliez et al. (1998) have demonstrated the connection between the laminar-to-turbulent transition of the near surface current and the first visual appearance of surface roughness. Kahma and Donelan observed surface waves at much lower wind speeds than our threshold wind speeds but were not able to determine the wavelengths of these disturbances (Kahma and Donelan, 1988). From observations using the wavelet technique, we have been able to determine that these initial disturbances are predominantly about 8 cm long, much longer than the waves studied here. We will discuss this in more detail in Part 2. For now, the data shown in Figures 2, 10, and 11 clearly show that gravity-capillary waves with spectral densities greater than  $10^{-5}$  times their equilibrium value are not present on the water surface below the threshold wind speed.

We now consider how the initial roughness at our Bragg wavelengths could have developed. As the wind stress on the surface builds up, the flow beneath the surface accelerates and attains ever higher Reynolds numbers. Eventually the flow becomes unstable, turbulent eddies begin to grow and, as they interact with the surface, produce deflections in the surface that modulate the airflow, producing pressure disturbances in the air that act to amplify the deflections and begin the rapid 'positive feedback' process of wave growth.

In these experiments we made no measurements of the flow field beneath the surface. In lieu of these we construct a model of the flow in a linear tank and apply the resulting flow structure to elucidate our measurements of wave growth. By virtue of the simple geometry, we neglect all lateral gradients and all longitudinal gradients of the flow, but retain the overall lengthwise pressure gradient that arises through the mass transport of fluid driven by the wind stress. The flow equation to be integrated is therefore:

$$\frac{\partial u}{\partial t} = -\frac{1}{\rho_w} \frac{\partial p}{\partial x} + \frac{1}{\rho_w} \frac{\partial \tau}{\partial z}. \quad (16)$$

Assuming that any loss of water through evaporation is negligible, mass conservation yields:

$$\frac{\partial u}{\partial t} = -\frac{8g}{L^2} \int \int u \, dz \, dt + \frac{\partial}{\partial z} \left[ (\nu + D) \frac{\partial u}{\partial z} \right]. \quad (17)$$

where  $L$  is the total length of the tank,  $z$  is positive upwards,  $\nu$  is the kinematic viscosity and  $D$  the eddy viscosity. The value of  $D$  is taken to be 0 when the local value of the Reynolds

number,  $Re$  is less than  $N$ , which is to be determined. Otherwise:

$$D = 0.4 * u_*(z)\zeta(z) \quad (18)$$

where  $\zeta$  is the nearer distance to surface or bottom.

The boundary conditions are the measured wind stress at the surface and  $u = 0$  on the bottom and (17) is integrated with a time step of 0.01 seconds. There are 27 levels spaced logarithmically from the top at 0.12 cm to 22.2 cm on the bottom.

The model was applied with the measured surface stress and the results are compared in Figure 13 with the observed time delays from runs such as those shown in Figures 10 and 11. The circles indicate the delay time between the wind reaching the threshold and the radar cross section reaching -50 dB. The asterisks indicate the time differences between the wind speed reaching threshold and the time when the Reynolds number in the model exceeds 130 anywhere in the upper part of the wind driven flow. Generally, the downwind flow near the surface occupied about 5 cm with the other 17 cm given over to the slow pressure driven return. The results are sensitive to the choice of 'critical Reynolds number' and the excellent agreement between measured delays and the transition of the Reynolds number above critical suggests that near this critical Reynolds number the flow becomes turbulent enough to disturb the nearby surface and initiate the amplification of waves by wind. The dashed line in Figure 13 is  $t_d = 110/U_{max}^2$ , showing that the delay time is inversely proportional to the maximum wind speed squared. This suggests that the initial acceleration of the near surface flow is proportional to the wind speed squared, or the surface stress.

With this fit to the delay times in the sudden start/stop mode, it is straightforward to compute the expected threshold wind speeds in the ramped mode for various ramp rates and an increasing wind speed. Thus if wind speed is proportional to the time as

$$U(t) = (dU/dt)t \quad (19)$$

where  $dU/dt$  is the constant ramp rate, then the average time delay over the time period  $T$  is

$$\langle t_d \rangle = 110 \int_0^T U^{-2}(t)dt/T. \quad (20)$$

where  $t = 0$  is the time of the threshold for a constant wind. When  $\langle t_d \rangle = T$ , gravity-capillary waves will begin to grow. We define  $U(T)$  to be the threshold wind speed for that ramp rate. Figure 14 compares these calculated threshold wind speeds (line) with those measured for  $k_b = 335$  rad/m (circles) and  $k_b = 415$  rad/m (squares). The agreement is sufficiently good to support the hypothesis that the delay awaiting the laminar-to-turbulent transition of the subsurface flow is the cause of the variable wind speed threshold. The threshold wind speed for constant wind speed was taken to be 1.65 m/s at 3 cm height for these comparisons. Figure 3 shows that the corresponding threshold friction velocity is about 0.07 m/s. Using these two values the equivalent wind speed at 10 m over the ocean would be 2.65 m/s at these water temperatures.

## 7 Conclusions

The concept of a threshold wind speed, below which no free (directly wind generated) gravity-capillary waves exist, has been verified using laboratory data on radar scattering at Ku-band as well as estimates of wavenumber spectra by a wavelet technique applied to laser measurements. The concept, advanced by Donelan and Pierson (1987), raises questions about the interpretation of microwave scatterometer data in light winds since most operational model functions do not include threshold effects, although recent papers by Plant [2000] and Shankaranarayanan and Donelan [2001] seek to rectify this. Furthermore, these experiments have shown that the threshold wind speed is dependent on the viscosity of the water, which is a strong function of temperature. The threshold friction velocity, however, showed no dependence on water temperature. This implies that radar cross sections and gravity-capillary wave spectral densities at low winds are proportional to the friction velocity in the absence of long waves. The experiments were done both at quasi steady state, in which the wind speed was allowed to rise to a preset maximum and then to fall to calm and under conditions of suddenly started and stopped winds. Experiments, in which the rate of change of wind speed was relatively high, showed a marked hysteresis in the response, with higher winds being required to generate waves on the rising wind and lighter winds being required to maintain them on the falling wind. We ascribe the former to the need to produce initial wavelets before they can be amplified by the feedback mechanisms, and the latter to the persistence of bound harmonics of the longer waves or the flux of energy from long to short waves through nonlinear wave interactions. Turbulent currents, however, increased the wind speed threshold by more than their speed, suggesting that while some turbulence is necessary for wave generation, too much turbulence damps short waves. Effects ascribable to bound harmonics or nonlinear interactions were observed as a reduction in the rate of decay of short waves below their viscous dissipation rate when the wind was suddenly stopped. Growth rates measured when the wind was suddenly started confirmed the similarity of Plant's growth rate formulation and that of Donelan and Pierson. The observations of the effect of water temperature on the thresholds and the fact that Plant's growth rate always predicted a higher threshold than observed lead us to conclude that wind speed near the surface is the parameter determining wave growth. Wind speed is a condition imposed on the air-water interface; friction velocity is a result of the air-water interaction.

## 8 Acknowledgements

The authors would like to thank Bill Keller, Ken Hayes, and Vahid Hesany for their help in carrying out these experiments. They would also like to thank the staff of the National Water Research Institute, in particular, D.C. Beesley, who operated the wind wave tank. The project was funded by NSF grant OCE 9402852AM01 and ONR grants N00014-93-1-0016 and N00014-00-1-0075.

## 9 References

- Belcher S.E., Wave growth by non-separated sheltering, *Eur J. Mech B-Fluid*, 18(3), 447-462, 1999.
- Belcher S.E. and J.C.R. Hunt, Turbulent shear-flow over slowly moving waves, *J. Fluid, Mech.*, 251, 109-148, 1993.
- Caulliez, G., N. Ricci and R. Dupont, The generation of the first visible wind waves, *Phys. Fluids*, 10, 757-759, 1998.
- Cohen, J.E. and S.E. Belcher, Turbulent shear flow over fast-moving waves, *J Fluid, Mech.*, 386, 345-371, 1999.
- Dobson, F.W., Measurements of atmospheric pressure on wind-generated sea waves. *J. Fluid Mech.*, 48(pt. 1), 91-127, 1971.
- Donelan, M.A., J. Hamilton, and W.H. Hui, Directional spectra of wind-generated waves, *Phil. Trans. R. Soc. Lond., A* 315, 509-562, 1985.
- Donelan, M.A. and W.J. Pierson, Jr., Radar scattering and equilibrium ranges in wind-generated waves with application to scatterometry, *J. Geophys. Res.*, 92 (C5), 4971-5029, 1987.
- Donelan M.A., W.M. Drennan and A.K. Magnusson, Nonstationary analysis of the directional properties of propagating waves, *J. Phys. Ocean.* 26 (9), 1901-1914, 1996.
- Elliott, J.A., Microscale pressure fluctuations near waves being generated by the wind. *J. Fluid Mech.*, 54(pt. 3), 427-448, 1972.
- Hara, T., E.J. Bock, and M. Donelan, Frequency-wavenumber spectrum of wind-generated gravity-capillary waves. *J. Geophys. Res.*, 102, 1061-1072, 1997.
- Hasselmann, K., T.P. Barnett, E. Bouws, H. Carlson, D.E. Cartwright, K. Enke, J.A. Ewing, H. Gienapp, D.E. Hasselmann, P. Kruseman, A. Meerburg, P. Müller, D. J. Olbers, K. Richter, W. Sell, H. Walden, Measurements of wind-wave growth and swell decay during the joint North Sea wave project. (JONSWAP). *Ergänzungsheft zur Deutschen Hydrograph. Zeitschrift*, **Reihe A** (8<sup>0</sup>)(12), 95 p., 1973.
- Jeffreys, H., On the formation of waves by wind, *Proc. Roy. Soc. London, Ser.A.*, 107, 189-206, 1924.



Jeffreys, H., On the formation of waves by wind II, Proc. Roy. Soc. London, Ser.A., 110, 341-347, 1925.

Kahma, K.K. and M.A. Donelan, A laboratory study of the minimum wind-speed for wind wave generation, J. Fluid Mech., 192, 339-364, 1988.

Kawai, S., Generation of initial wavelets by instability of a coupled shear flow and their evolution to wind waves. J. Fluid Mech., 93(pt. 4), 661-703, 1979

Keller, M.R., B.L. Gotwols, W.J. Plant, and W.C. Keller, Comparison of optically-derived spectral densities and microwave cross sections in a wind-wave tank, J. Geophys. Res., 100(C8), 16163-16178, 1995.

Larson, T.R. and J.W. Wright, Wind-generated gravity-capillary waves: Laboratory measurements of temporal growth rates using microwave backscatter, J. Fluid Mech., 97, 455-479, 1975.

Miles, J.W., On the generation of surface waves by shear flows, J. Fluid Mech., 3, 185-204, 1957.

Miles, J.W., On the generation of surface waves by shear flows, Part 2, J. Fluid Mech., 6, 568-582, 1959a.

Miles, J.W., On the generation of surface waves by shear flows, Part 3, J. Fluid Mech., 6, 583-598, 1959b.

Miles, J.W., On the generation of surface waves by turbulent shear flows, J. Fluid Mech., 7, 469-478, 1960.

Miles, J.W., On the generation of surface waves by shear flows. Part 4, J. Fluid Mech., 13, 433-448, 1962.

Miles, J.W., Surface-wave generation revisited, J. Fluid Mech., 256, 427-441, 1993.

Mollochristensen, E., and A. Ramamonjiarisoa, Sub-harmonic transitions and group formation in a wind wave field, J. Geophys. Res., 87(C8), 5699-5717, 1982.

Plant, W.J., On the energy balance of short gravity wave systems. J. Phys. Oceanog., 10(9), 1340-1352, 1980.

Plant, W.J., A relationship between wind stress and wave slope, J. Geophys. Res., 87 (C3), 1961-1967, 1982.

- Plant, W.J., A two-scale model of short, wind-generated waves and scatterometry, *J. Geophys. Res.*, 90 (C9), 10735-10749, 1986.
- Plant, W.J., Bragg scattering of electromagnetic waves from the air /sea interface, in Surface Waves and Fluxes: Current Theory and Remote Sensing. Edited by G.L. Geernaert and W.J. Plant, Kluwer Academic Publishers, 2, 41-108, 1990.
- Plant, W.J., J.W. Wright, Phase speeds of upwind and downwind traveling short gravity waves. *J. Geophys. Res.*, 85(C6), 3304-3310, 1980.
- Plant, W.J., Keller, W.C., R.A. Petitt, and E.A. Terray, The dependence of microwave backscatter from the sea on illuminated area: Correlation times and lengths, *J. Geophys. Res.*, 99(C5), p. 9705-9723, 1994.
- Plant, W.J., D.E. Weissman, W.C. Keller, V. Hesany, K. Hayes, and K.W. Hoppel, Air/sea momentum transfer and the microwave cross section of the sea, *J. Geophys. Res.*, 104(C5), 11173-11191, 1999a.
- Plant, W.J., W.C. Keller, V. Hesany, T. Hara, E. Bock, and M. Donelan, Bound waves and Bragg scattering in a wind wavetank, *J. Geophys. Res.*, 104(C2), 3243-3263, 1999b.
- Plant, W.J., W.C. Keller, V. Hesany, K. Hayes, Peter Dahl, T. Hara, E. Bock, and M. Donelan, "Crumpling" wave effects in backscatter from the air-sea interface., *Proceedings of the Sydney Air/Sea Interaction Symposium*. Edited by Michael Banner. 1999c.
- Plant, W.J., Effects of wind variability on scatterometry at low wind speeds, *J. Geophys. Res.*, 105(C7), 16,899-16,910, 2000.
- Riley, D.S., M.A. Donelan, and W.H. Hui, An extended miles' theory for wave generation by wind, *Bdry Layer Met.*, 22, 209-225, 1982.
- Shankaranarayanan, K. and M.A. Donelan, A probabilistic approach to scatterometer model function verification, *J. Geophys. Res.*, 106(C9), 19,969-19,990, 2001.
- Shemdin, O.H. and E.Y. Hsu, 1967. Direct measurement of aerodynamic pressure above a simple progressive gravity wave. *J. Fluid Mech.*, 30(pt. 2), pp. 403-416, 1967.
- Snyder, R.L., A field study of wave-induced pressure fluctuations above surface gravity waves. *J. Mar. Res.*, 32(3), 497-531, 1974.
- Snyder, R.L., F.W. Dobson, J.A. Elliott, and R.B. Long, Array measurements of atmospheric

pressure fluctuations above surface gravity waves. *J. Fluid Mech.*, 102, 1-59, 1981.

Uz, B.M., Gravity-capillary waves and their influence on air-sea interaction under non-stationary conditions, Ph.D. thesis, University of Rhode Island. 163pp. 1999.

Uz, B.M., M.A. Donelan, T. Hara and E.J. Bock, Laboratory studies of wind stress over surface waves, *Boundary-Layer Meteorology*, 102, 301-331, 2002a.

Uz, B.M., T. Hara, E.J. Bock and M.A. Donelan, Laboratory observations of gravity-capillary under transient wind forcing, *J. Geophys. Res.* (in press), 2002b.

Veron, F., and W.K. Melville, Experiments on the stability and transition of wind-driven water surfaces, *J. Fluid Mech.*, 446, 25-65, 2001.

Valenzuela, G.R., The growth of gravity-capillary waves in a coupled shear flow, *J. Fluid Mech.*, 76. 229-250, 1976

Wu, H.Y., E.Y. Hsu, and R.L. Street, Experimental study of nonlinear wave-wave interaction and white-cap dissipation of wind-generated waves, *Dyn. Atmos. Oceans*, 3, 55-78, 1979.

## 10 Figure Captions

Figure 1. Diagram of the CCIW wind wave tank showing the placement of instruments.

Figure 2. a) Time plot of wind speed at 3 cm (solid line) and friction velocity at the surface (dashed line) for a slowly ramped wind (ramp rate = 0.34 cm/s/s). b) Time plot of  $F(k_b, 0)$  from Ku band radar cross sections and  $F(k_b, 0)$  from the laser height/slope gauge, where  $k_b = 335$  rad/m. The radar antenna was at a  $35^\circ$  incidence angle looking upwind. The fetch at the radar footprint was 10.0 m while the fetch was 14.3 m to the laser probe. Solid curve - radar, VV; dashed curve - radar, HH; asterisks - laser.

Figure 3. Ku band radar cross section,  $\sigma_o$ , and  $F(k_b, 0)$  from the laser versus wind. Data are the same as those shown in Figure 2. Squares, asterisks = upramp; circles, pluses = downramp; dashed lines = Donelan/Pierson model, solid lines = Plant model. a)  $\sigma_o(VV)$  versus  $u_*$ , b)  $\sigma_o(VV)$  versus  $U(3\text{cm})$ , c)  $F(k_b, 0)$  versus  $u_*$ , d)  $F(k_b, 0)$  versus  $U(3\text{cm})$ .

Figure 4. Ku band cross sections,  $\sigma_o$ , at different fetches for a slowly increasing wind versus (a) friction velocity and (b) wind speed at 3 cm. Rate of change of wind speed is 0.3 cm/s/s. Symbols are as follows: squares =  $\sigma_o$  (VV), downwind, 7.4 m fetch; pluses =  $\sigma_o$  (VV), upwind, 10.0 m fetch; circles =  $\sigma_o$  (VV), downwind, 12.4 m fetch; diamonds = spectral densities from laser converted to  $\sigma_o$  (VV), 14.3 m fetch. Radar is at a  $45^\circ$  incidence angle,

$k_b = 415$  rad/m.

Figure 5. Ku band cross sections,  $\sigma_o$ , at different fetches for a slowly decreasing wind versus (a) friction velocity and (b) wind speed at 3 cm. Rate of change of wind speed is 0.3 cm/s/s. Parameters as in Figure 4 except that no data were taken at 12.4 m fetch.

Figure 6. Ku band cross sections,  $\sigma_o$ , at different fetches for an increasing wind versus (a) friction velocity and (b) wind speed at 3 cm. Rate of change of wind speed is 2.7 cm/s/s. Symbols are as follows: squares =  $\sigma_o$  (VV), upwind, 10.0 m fetch; circles =  $\sigma_o$  (VV), downwind, 12.4 m fetch; asterisks = spectral densities from laser converted to  $\sigma_o$  (VV), 14.3 m fetch. Radar is at a 45° incidence angle,  $k_b = 415$  rad/m.

Figure 7. Ku band cross sections,  $\sigma_o$ , at different fetches for a decreasing wind versus (a) friction velocity and (b) wind speed at 3 cm. Rate of change of wind speed is 2.7 cm/s/s. Parameters as in Figure 6.

Figure 8. Ku band radar cross sections,  $\sigma_o$ , at two different water temperatures for a decreasing wind versus (a) friction velocity and (b) wind speed at 3 cm. Data taken in 1996 at a fetch of 10.0 m with an upwind look direction; incidence angle is 45° ( $k_b = 415$  rad/m). Rate of change of wind speed is 0.3 cm/s/s. Air temperatures were between 20°C and 22°C. Symbols indicate water temperature as follows: circles = 20.0°C, squares = 29.4°C.

Figure 9. Ku band radar cross sections with different currents and a decreasing wind versus (a) friction velocity, and (b) wind speed at 3 cm. Rate of change of wind speed was near 0.3 cm/s/s, air temperatures were about 22°, and water temperatures were between 18° and 21°. Symbols indicate different currents as follows: circles = 0 cm/s, squares = 12 cm/s, pluses = 27.6 cm/s. The antenna was directed upwind for the two lower currents (fetch = 10.0 m) and downwind for the higher (fetch = 7.4 m); the incidence angle was 45° ( $k_b = 415$  rad/m).

Figure 10. a) Time plot of wind speed at 4.7 cm and friction velocity for a suddenly started and stopped wind. Solid line = wind speed, dash-dotted line = friction velocity times 10. b) Time plot of  $F(k_b, 0)$  from Ku band radar cross sections and  $F(k_b, 0)$  from laser height/slope gauge for  $k_b = 335$  rad/m. The radar antenna was directed upwind at a 35° incidence angle. Solid curve - radar, VV; dashed curve - radar, HH; circles (error bars indicate integration time) - laser; heavy dashed line = wave growth from (10) with Donelan/Pierson's growth rate, (2); heavy solid line = wave growth from (10) with Plant's growth rate, (1); heavy dash-dotted line = decay due to viscosity.

Figure 11. Same as Figure 10 but for a lower maximum wind speed.

Figure 12. a) Wave decay rates versus maximum wind speed at 3 cm for  $k_b = 415$  rad/m. Asterisks are measured fast decay rate, triangles are measured slow decay rate, solid line

is viscous decay at 415 rad/m. b) Same as a) but for  $k_b = 335$  rad/m. c) Growth rates versus maximum wind speed at 3 cm for  $k_b = 415$  rad/m. Asterisks are measured growth rates, squares are growth rates from Plant's equation, (1), circles are growth rates from Donelan/Pierson's equation, (2). d) Same as c) but for  $k_b = 335$  rad/m.

Figure 13. Comparison of the delay time between the time the suddenly started wind reaches the threshold wind speed and the time the radar cross section reaches -50 dB (circles). The asterisks indicate the time differences between the time the wind reaches threshold and the time at which the Reynolds number in the model crossed 130 anywhere in the upper part of the wind driven flow. The dashed line is  $110/U_{max}^2$ ,  $U_{max}$  is the maximum wind speed [m/s] after a suddenly started wind.

Figure 14. Comparison of predicted threshold wind speeds for various ramp rates and an increasing wind with measured threshold wind speeds. Threshold was defined to be the wind speed at which the radar cross section reached -50 dB. The line is the predicted threshold using the fit to the data of Figure 13. Circles are for  $k_b = 335$  rad/m while squares are for  $k_b = 415$  rad/m.

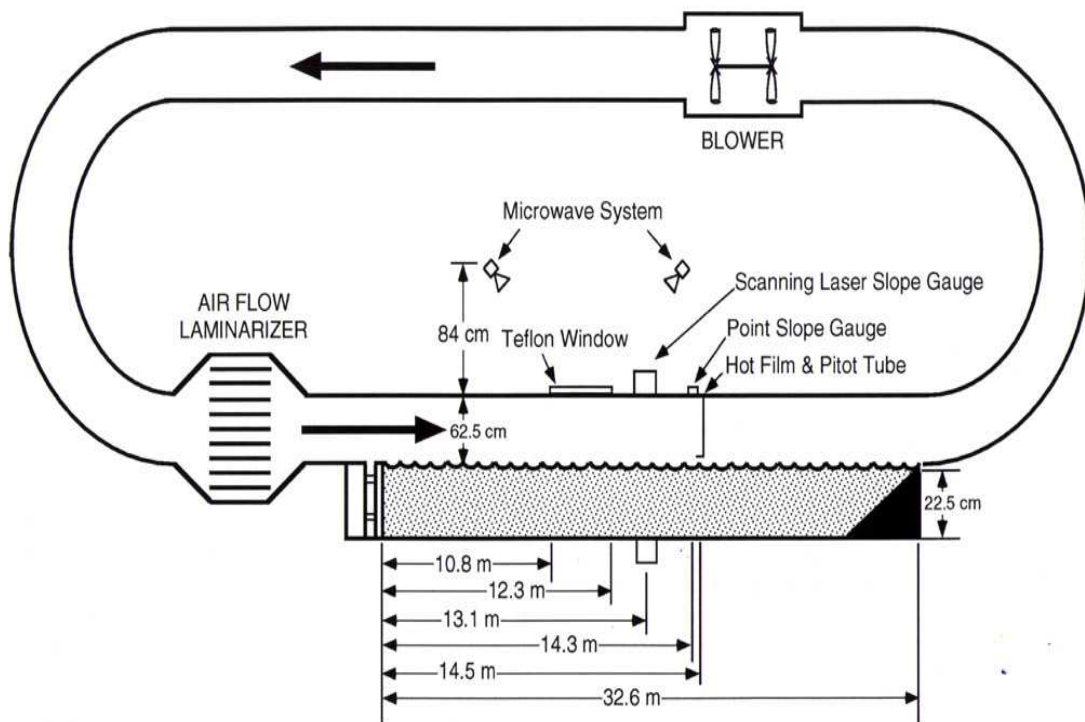


Figure 1: Diagram of the CCIW wind wave tank showing the placement of instruments.

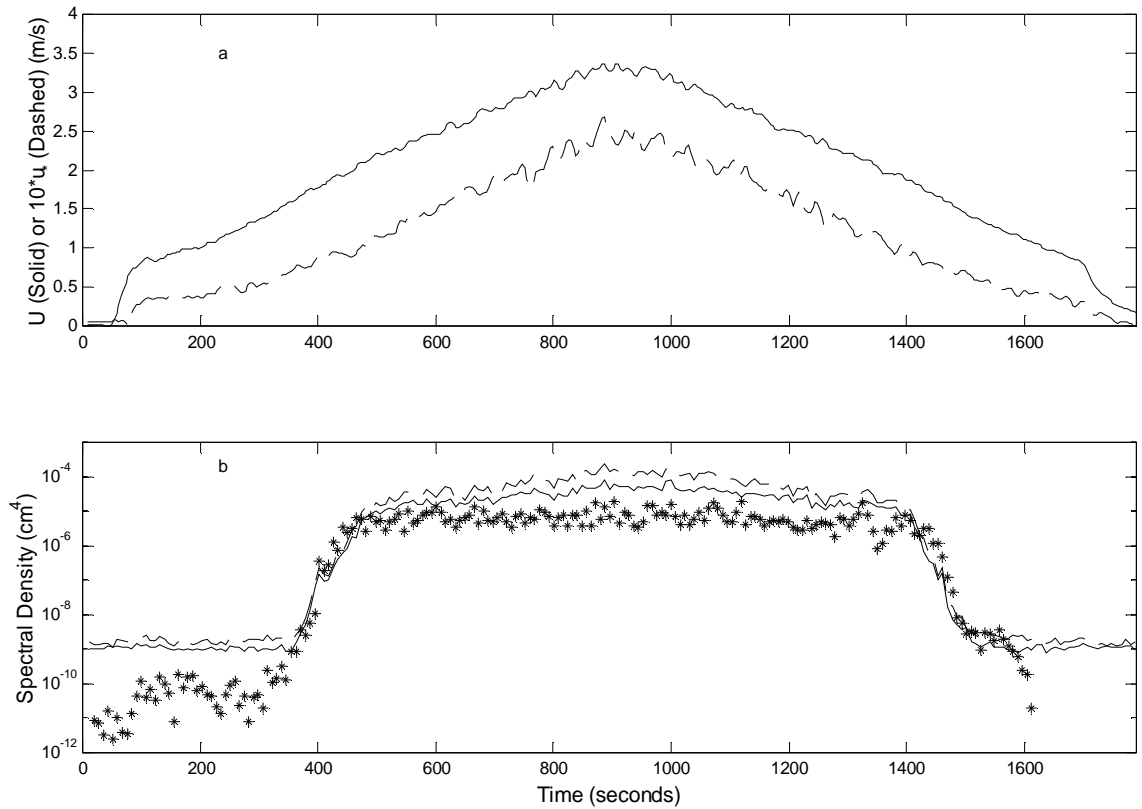


Figure 2: a) Time plot of wind speed at 3 cm (solid line) and friction velocity at the surface (dashed line) for a slowly ramped wind (ramp rate = 0.34 cm/s/s). b) Time plot of  $F(k_b, 0)$  from Ku band radar cross sections and  $F(k_b, 0)$  from the laser height/slope gauge, where  $k_b = 335$  rad/m. The radar antenna was at a  $35^\circ$  incidence angle looking upwind. The fetch at the radar footprint was 10.0 m while the fetch was 14.3 m to the laser probe. Solid curve - radar, VV; dashed curve - radar, HH; asterisks - laser.

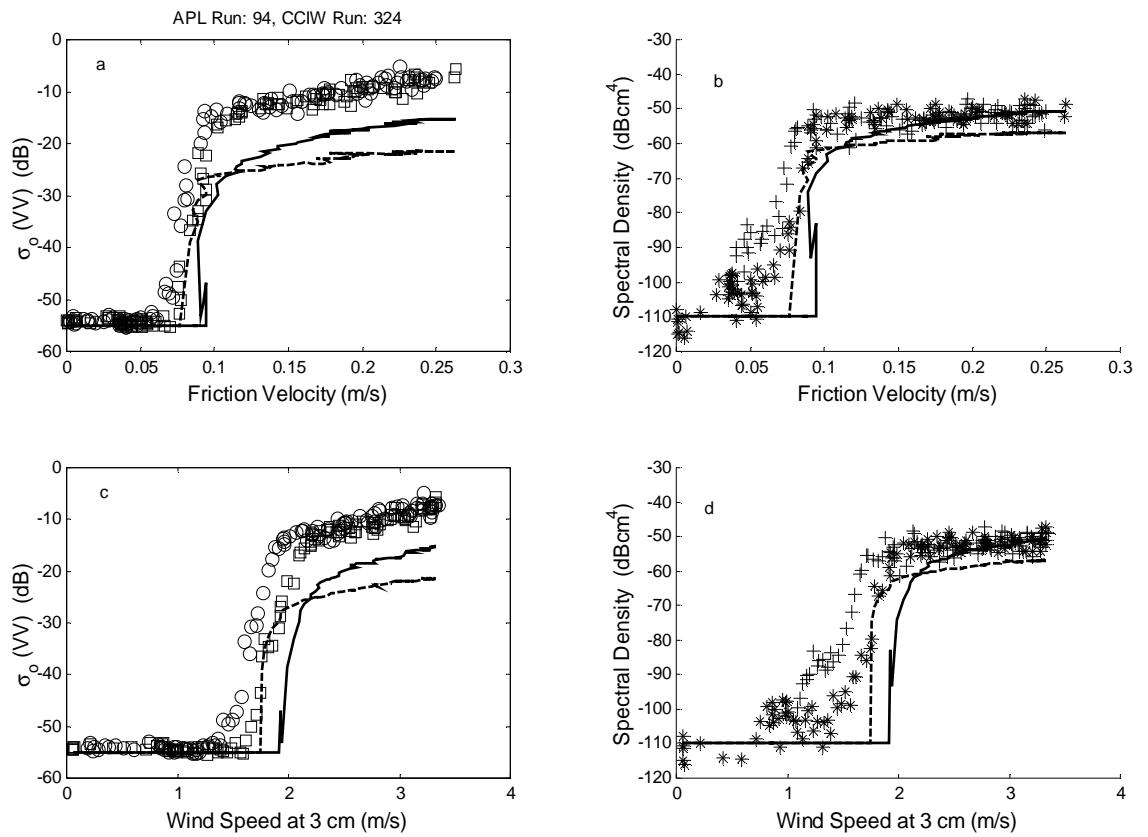


Figure 3: Ku band radar cross section,  $\sigma_o$ , and  $F(k_b, 0)$  from the laser versus wind. Data are the same as those shown in Figure 2. Squares, asterisks = upramp; circles, pluses = downramp; dashed lines = Donelan/Pierson model, solid lines = Plant model. a)  $\sigma_o(VV)$  versus  $u_*$ , b)  $\sigma_o(VV)$  versus  $U(3\text{cm})$ , c)  $F(k_b, 0)$  versus  $u_*$ , d)  $F(k_b, 0)$  versus  $U(3\text{cm})$ .



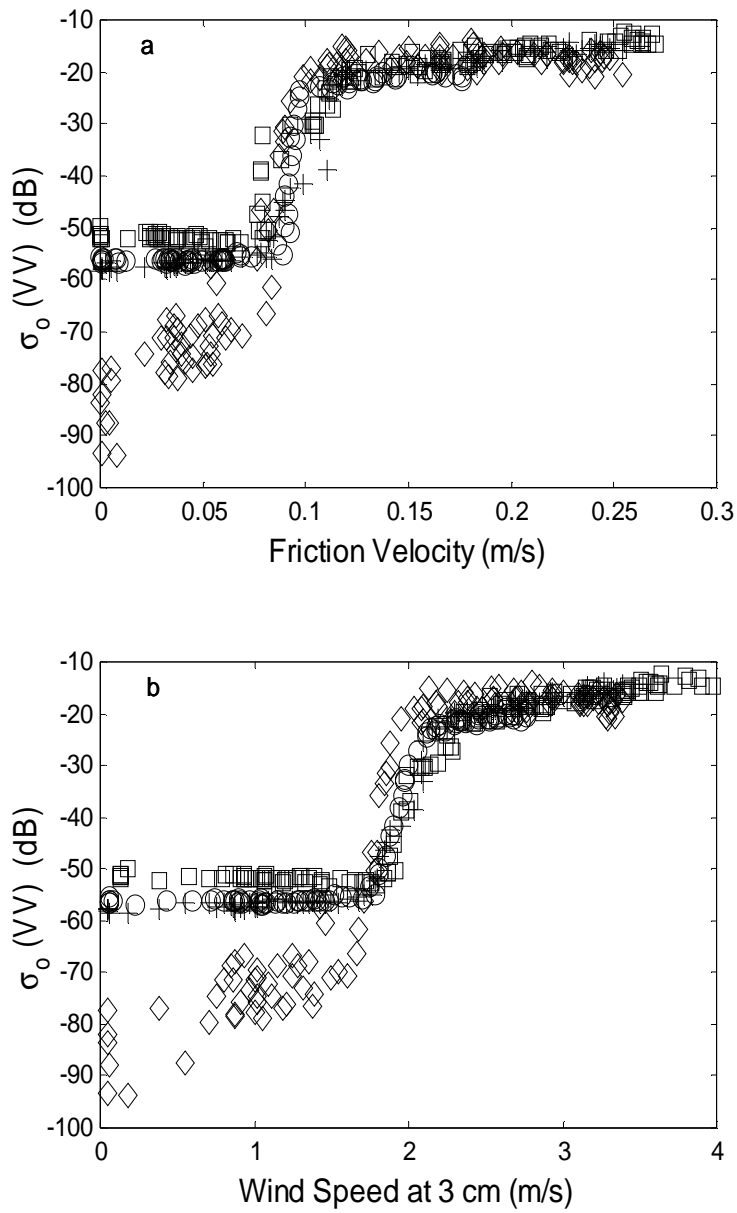


Figure 4: Ku band cross sections,  $\sigma_o$ , at different fetches for a slowly increasing wind versus (a) friction velocity and (b) wind speed at 3 cm. Rate of change of wind speed is 0.3 cm/s/s. Symbols are as follows: squares =  $\sigma_o$  (VV), downwind, 7.4 m fetch; pluses =  $\sigma_o$  (VV), upwind, 10.0 m fetch; circles =  $\sigma_o$  (VV), downwind, 12.4 m fetch; diamonds = spectral densities from laser converted to  $\sigma_o$  (VV), 14.3 m fetch. Radar is at a 45° incidence angle,  $k_b = 415$  rad/m.

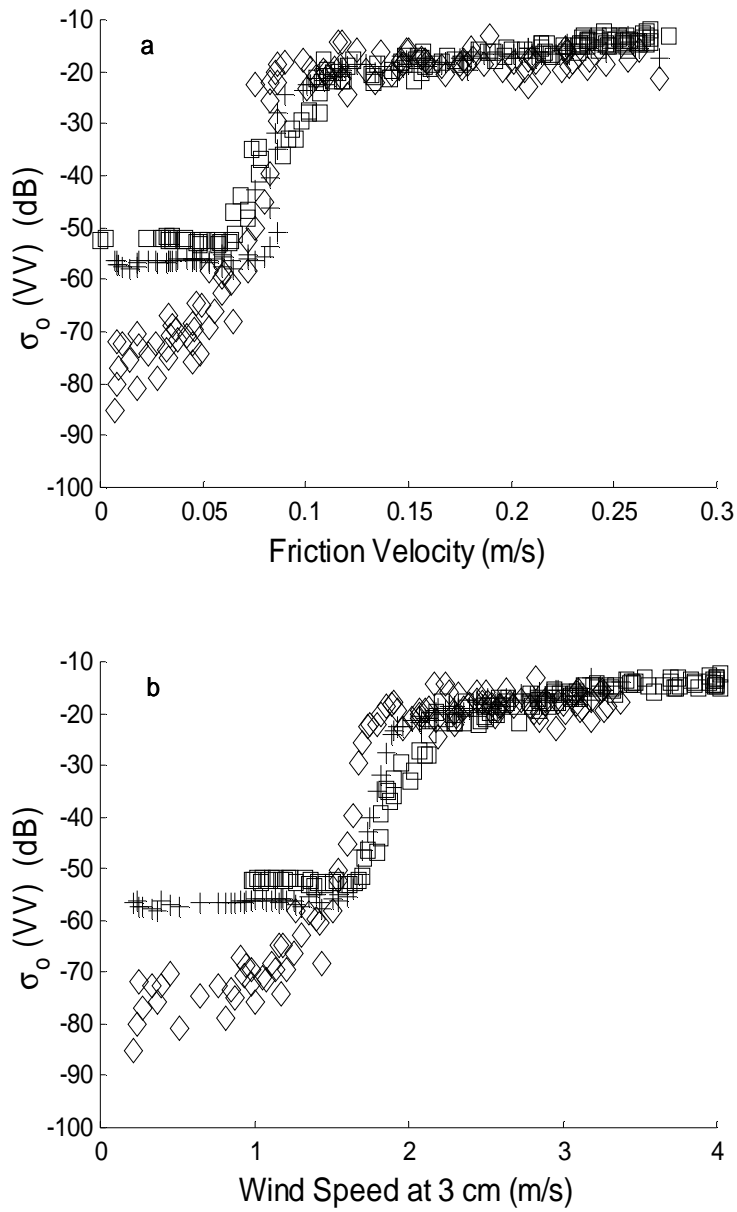


Figure 5: Ku band cross sections,  $\sigma_0$ , at different fetches for a slowly decreasing wind versus (a) friction velocity and (b) wind speed at 3 cm. Rate of change of wind speed is 0.3 cm/s/s. Parameters as in Figure 4 except that no data were taken at 12.4 m fetch.

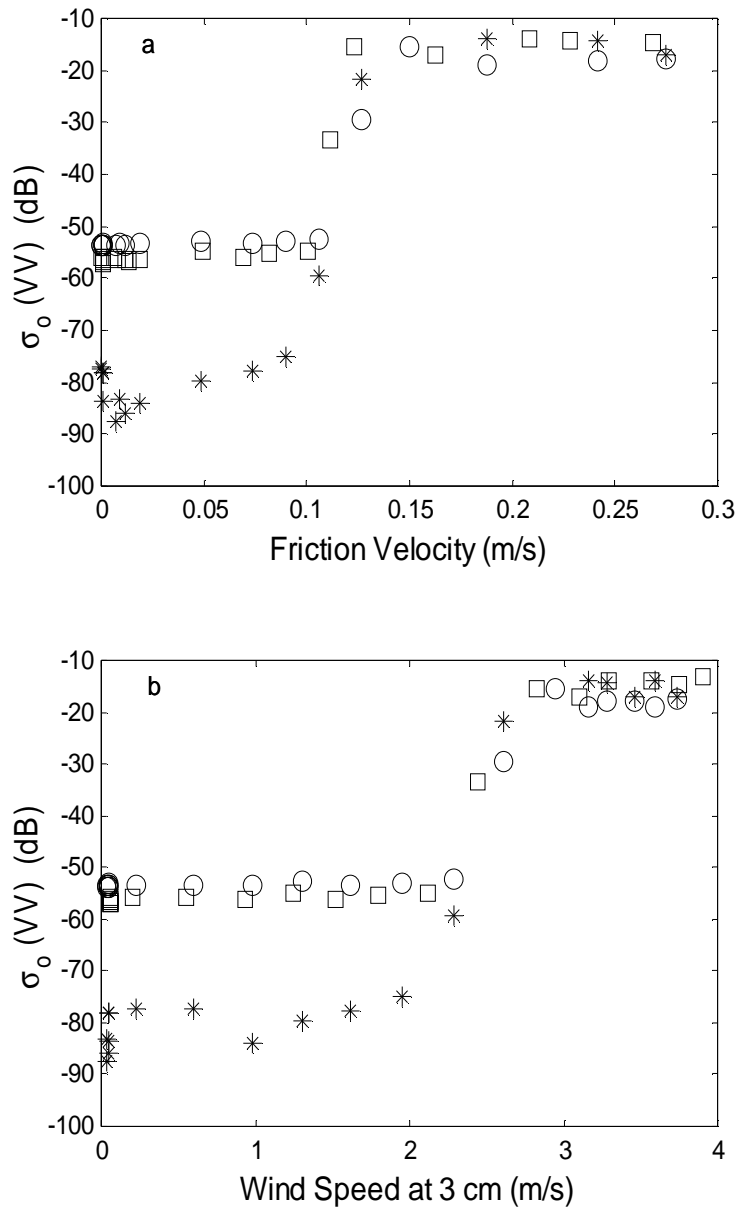


Figure 6: Ku band cross sections,  $\sigma_o$ , at different fetches for an increasing wind versus (a) friction velocity and (b) wind speed at 3 cm. Rate of change of wind speed is 2.7 cm/s/s. Symbols are as follows: squares =  $\sigma_o$  (VV), upwind, 10.0 m fetch; circles =  $\sigma_o$  (VV), downwind, 12.4 m fetch; asterisks = spectral densities from laser converted to  $\sigma_o$  (VV), 14.3 m fetch. Radar is at a  $45^\circ$  incidence angle,  $k_b = 415$  rad/m.

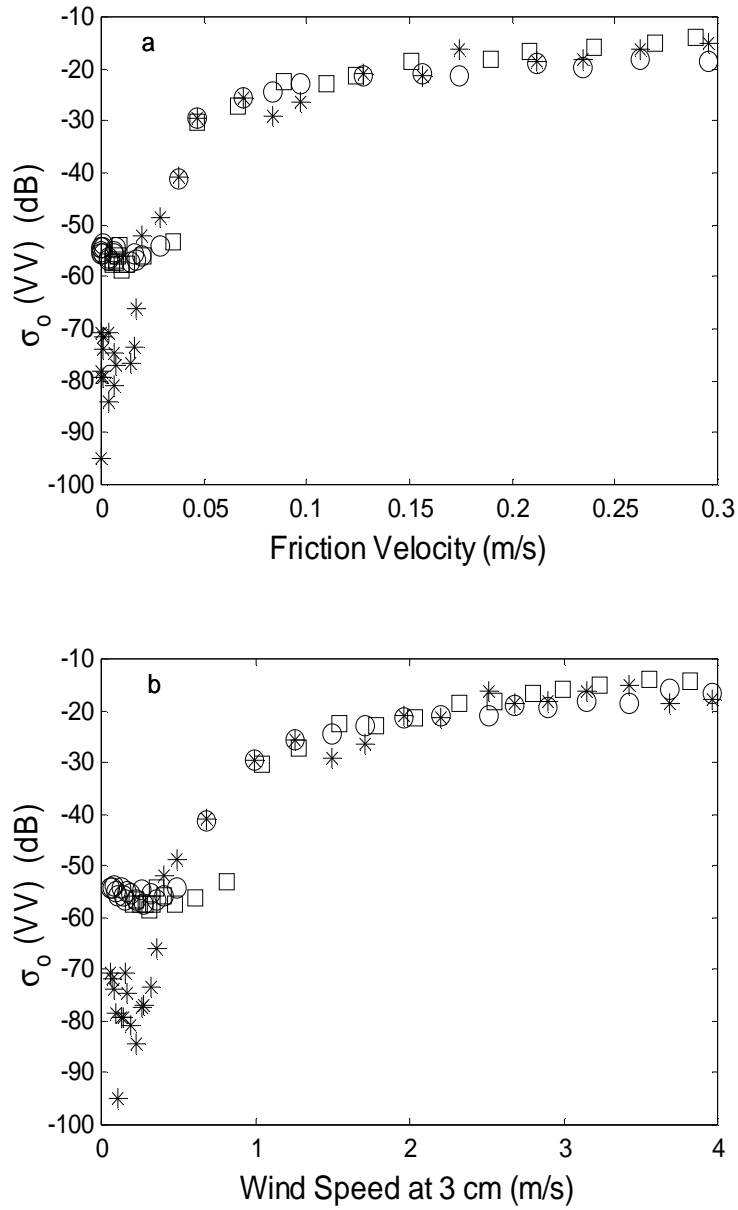


Figure 7: Ku band cross sections,  $\sigma_0$ , at different fetches for a decreasing wind versus (a) friction velocity and (b) wind speed at 3 cm. Rate of change of wind speed is 2.7 cm/s/s. Parameters as in Figure 6.

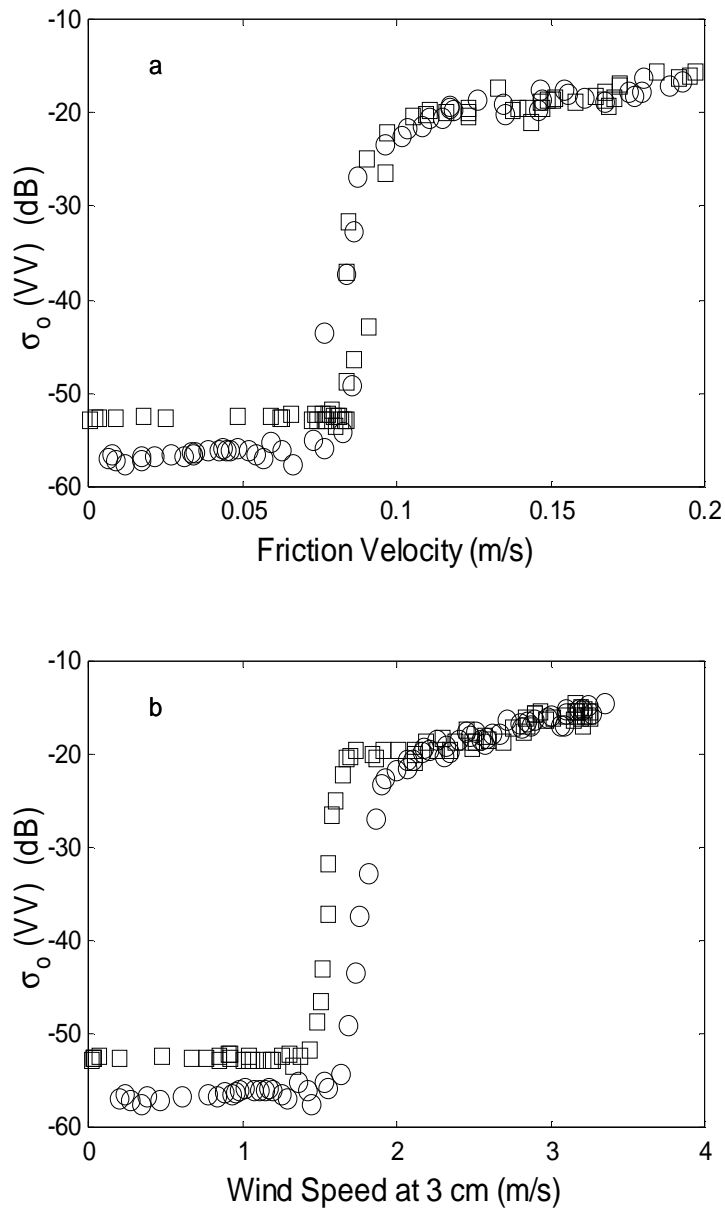


Figure 8: Ku band radar cross sections,  $\sigma_o$ , at two different water temperatures for a decreasing wind versus (a) friction velocity and (b) wind speed at 3 cm. Data taken in 1996 at a fetch of 10.0 m with an upwind look direction; incidence angle is  $45^\circ$  ( $k_b = 415$  rad/m). Rate of change of wind speed is 0.3 cm/s/s. Air temperatures were between  $20^\circ\text{C}$  and  $22^\circ\text{C}$ . Symbols indicate water temperature as follows: circles =  $20.0^\circ\text{C}$ , squares =  $29.4^\circ\text{C}$ .

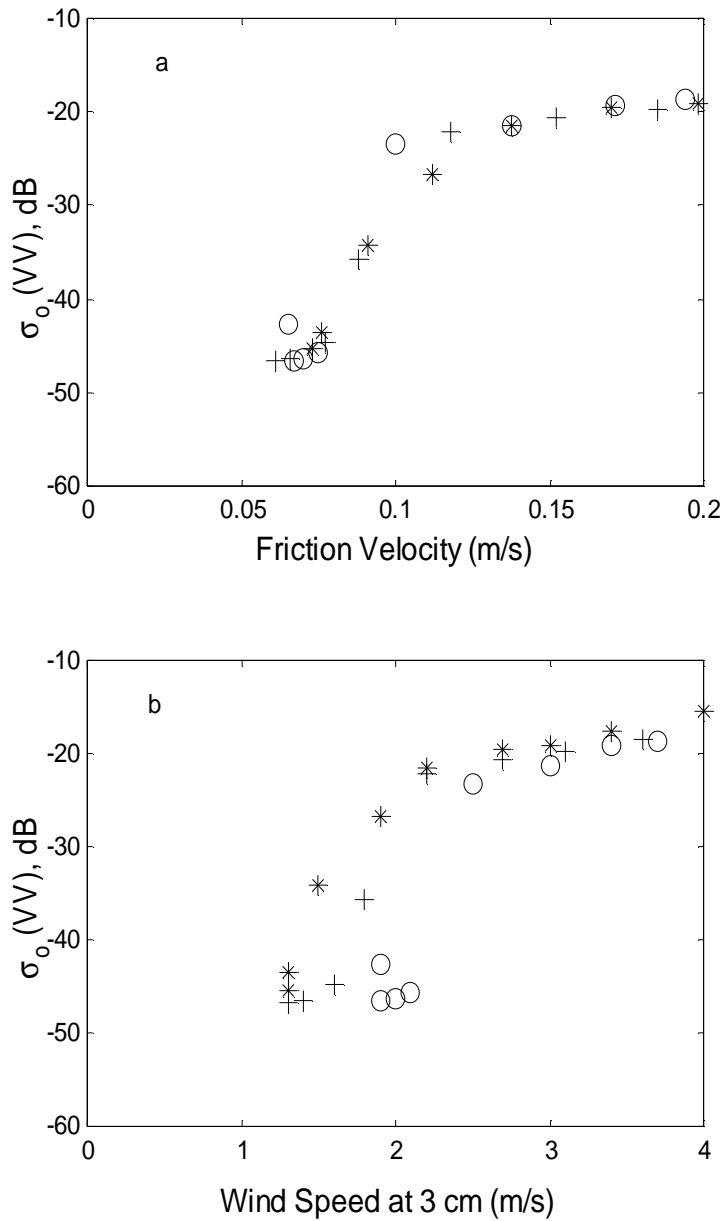


Figure 9: Ku band radar cross sections at two different water temperatures versus (a) friction velocity and (b) wind speed at 3 cm. Data taken in 1993 with different fixed wind speeds, a  $45^\circ$  incidence angle ( $k_b = 415$  rad/m), an upwind look and a fetch of 10 m. Air temperatures were between  $24^\circ\text{C}$  and  $25^\circ\text{C}$ . Symbols indicate water temperatures as follows: circles =  $10.2^\circ\text{C}$ , pluses =  $24.6^\circ\text{C}$ , asterisks =  $29.6^\circ\text{C}$ .

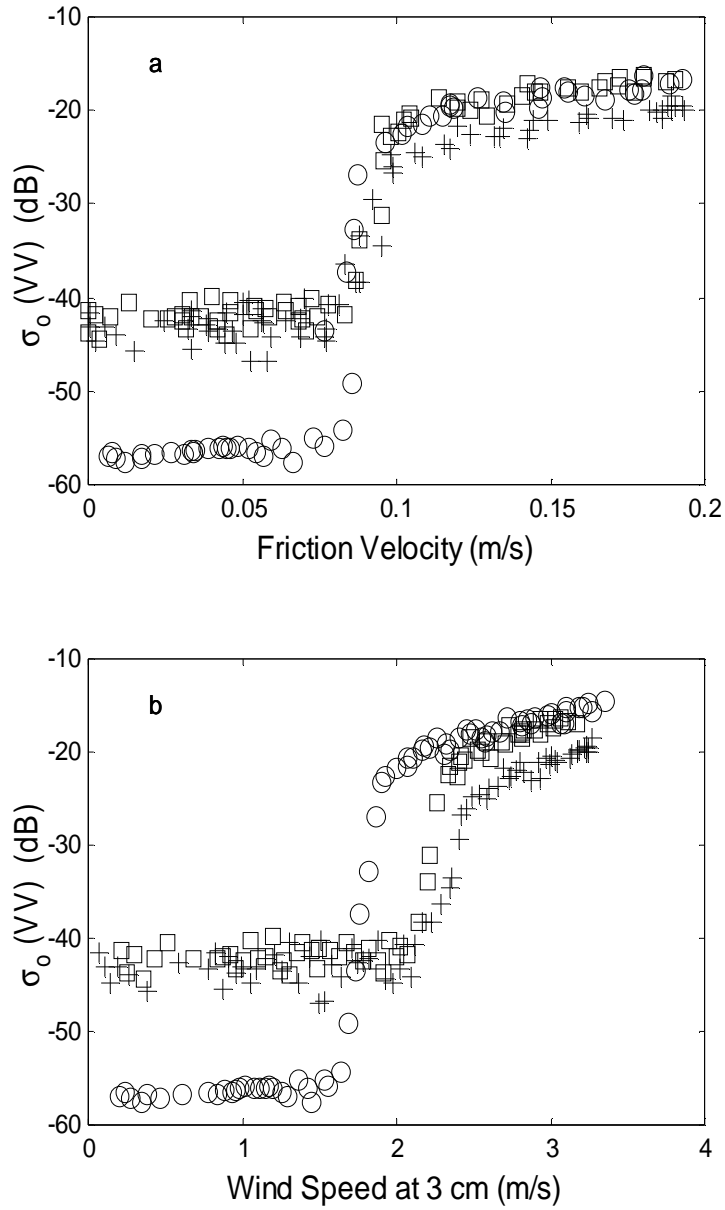


Figure 10: Ku band radar cross sections with different currents and a decreasing wind versus (a) friction velocity, and (b) wind speed at 3 cm. Rate of change of wind speed was near 0.3 cm/s/s, air temperatures were about 22°, and water temperatures were between 18° and 21°. Symbols indicate different currents as follows: circles = 0 cm/s, squares = 12 cm/s, pluses = 27.6 cm/s. The antenna was directed upwind for the two lower currents (fetch = 10.0 m) and downwind for the higher (fetch = 7.4 m); the incidence angle was 45° ( $k_b = 415$  rad/m).

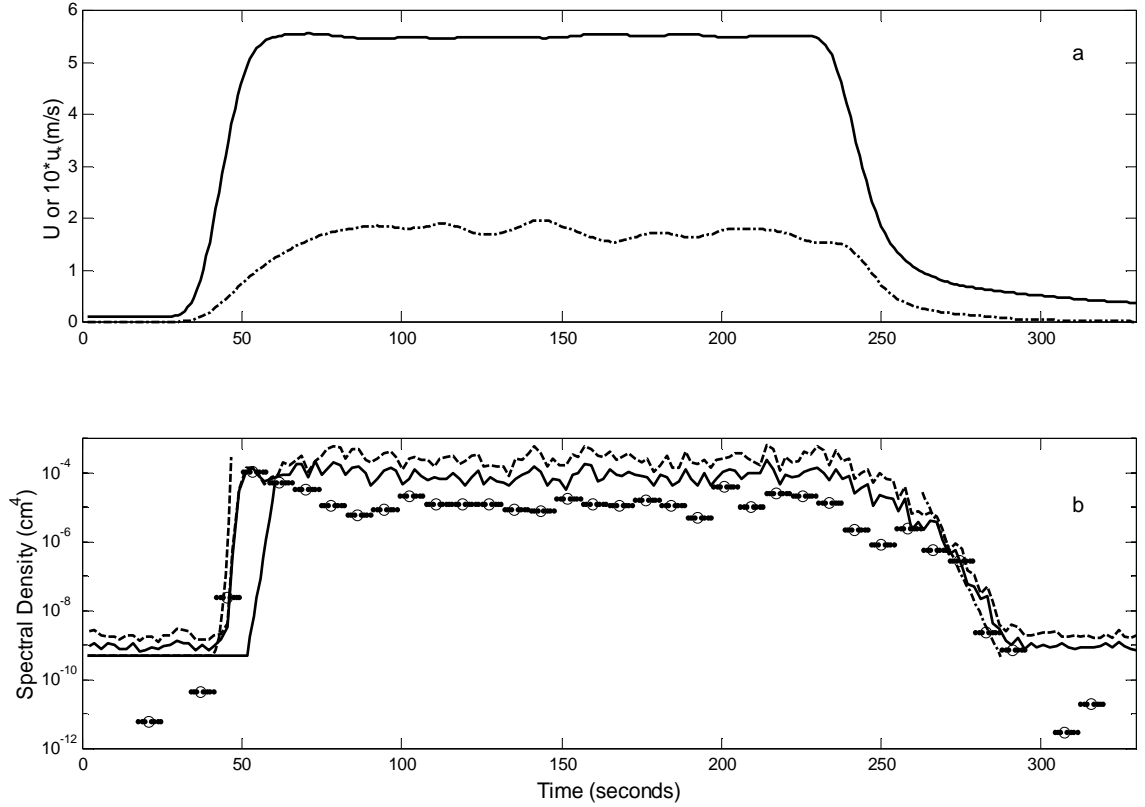


Figure 11: a) Time plot of wind speed at 4.7 cm and friction velocity for a suddenly started and stopped wind. Solid line = wind speed recorded on laser computer, dashed line = wind speed recorded on radar computer, dash-dotted line = friction velocity times 10. b) Time plot of  $F(k_b, 0)$  from Ku band radar cross sections and  $F(k_b, 0)$  from laser height/slope gauge for  $k_b = 335$  rad/m. The radar antenna was directed upwind at a  $35^\circ$  incidence angle. Solid curve - radar, VV; dashed curve - radar, HH; circles (error bars indicate integration time) - laser; heavy dashed line = wave growth from (10) with Donelan/Pierson's growth rate, (2); heavy solid line = wave growth from (10) with Plant's growth rate, (1); heavy dash-dotted line = decay due to viscosity.



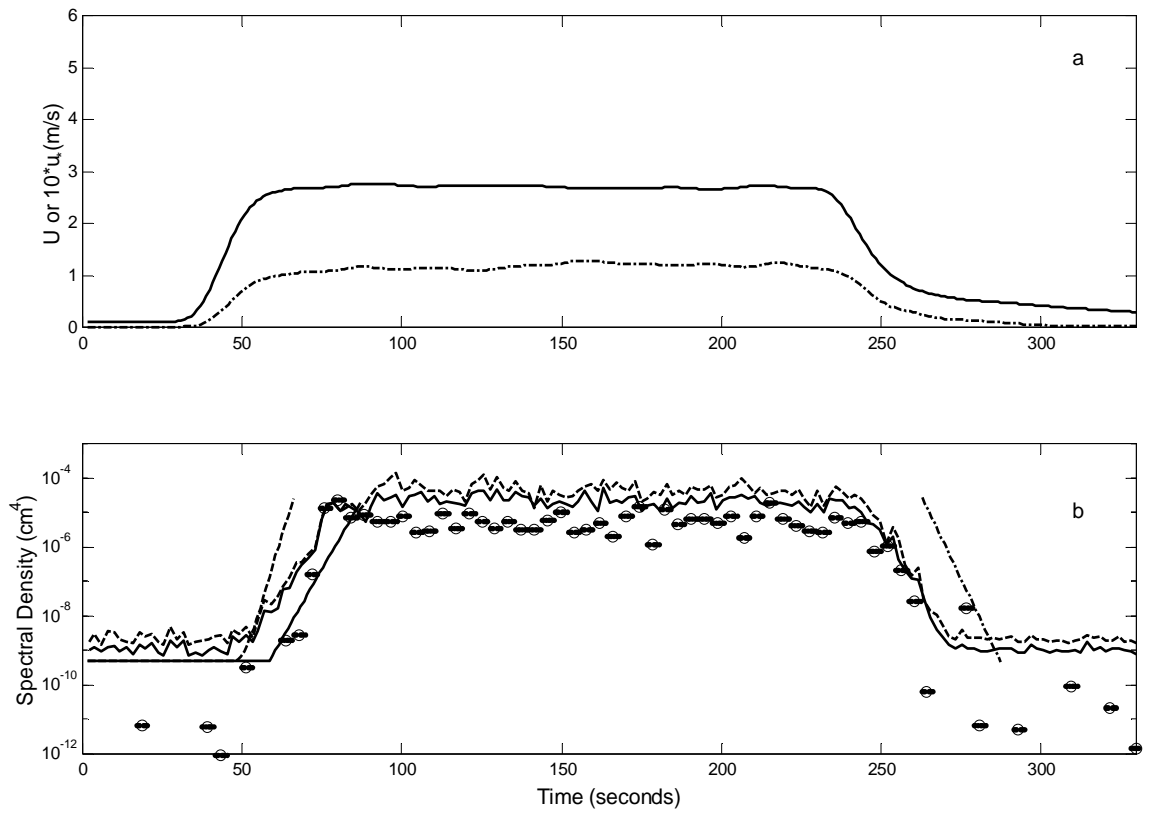


Figure 12: Same as Figure 11 but for a lower maximum wind speed.

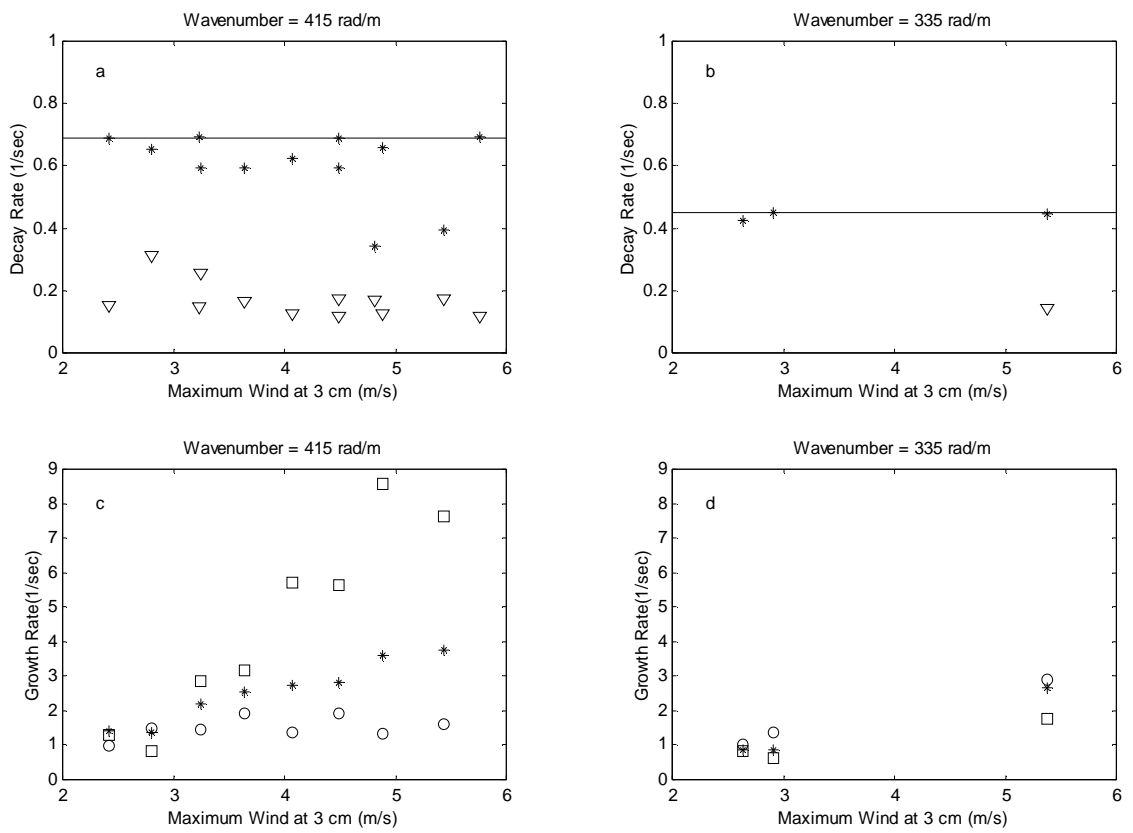


Figure 13: a) Wave decay rates versus maximum wind speed at 3 cm for  $k_b = 415$  rad/m. Asterisks are measured fast decay rate, triangles are measured slow decay rate, solid line is viscous decay at 415 rad/m. b) Same as a) but for  $k_b = 335$  rad/m. c) Growth rates versus maximum wind speed at 3 cm for  $k_b = 415$  rad/m. Asterisks are measured growth rates, squares are growth rates from Plant's equation, (1), circles are growth rates from Donelan/Pierson's equation, (2). d) Same as c) but for  $k_b = 335$  rad/m.

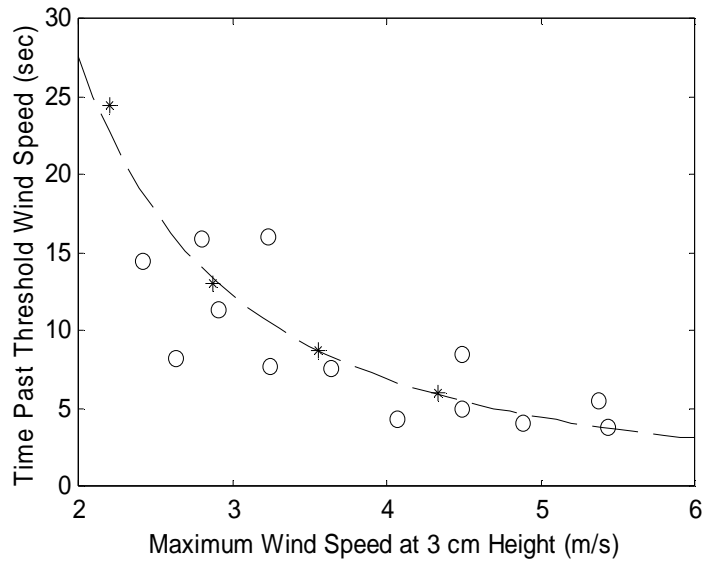


Figure 14: Comparison of the delay time between the time the suddenly started wind reaches the threshold wind speed and the time the radar cross section reaches -50 dB (circles). The asterisks indicate the time differences between the time the wind reaches threshold and the time at which the Reynolds number in the model crossed 130 anywhere in the upper part of the wind driven flow. The dashed line is  $110/U_{max}^2$ ,  $U_{max}$  is the maximum wind speed [m/s] after a suddenly started wind.

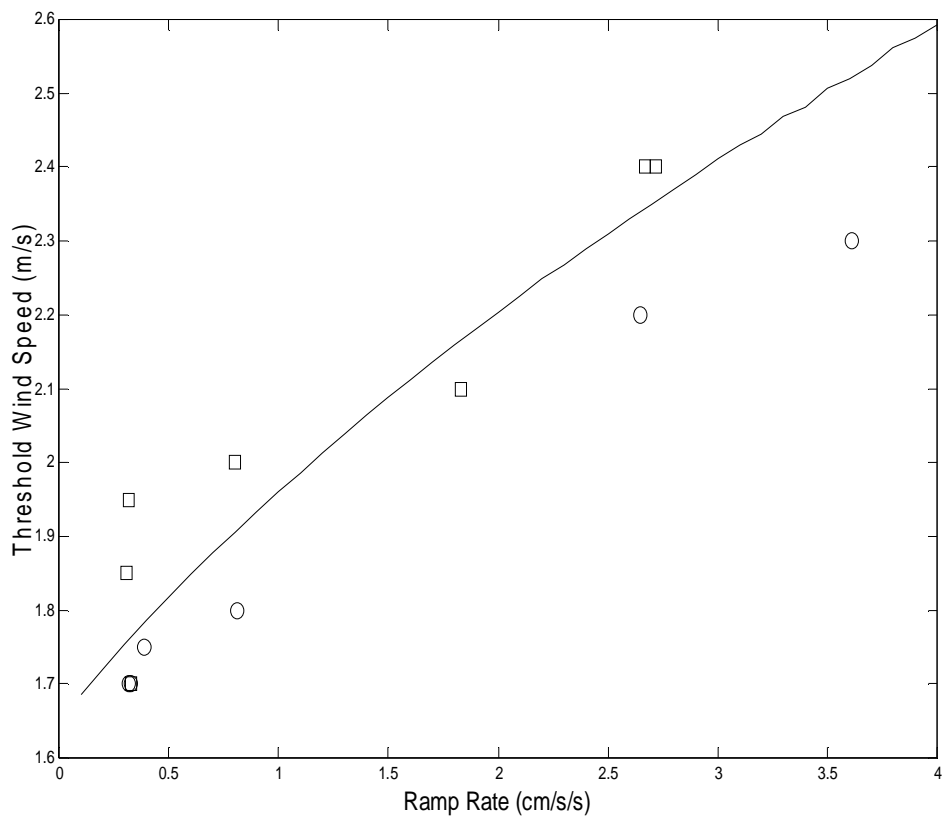


Figure 15: Comparison of predicted threshold wind speeds for various ramp rates and an increasing wind with measured threshold wind speeds. Threshold was defined to be the wind speed at which the radar cross section reached -50 dB. The line is the predicted threshold using the fit to the data of Figure 14. Circles are for  $k_b = 335$  rad/m while squares are for  $k_b = 415$  rad/m.